JOURNAL OF THERMOPHYSICS AND HEAT TRANSFER
Vol. 17, No. 3, July–September 2003

General Pressure-Correction Strategy to Include Density Variation in Incompressible Algorithms

Masoud Darbandi* and Seyed-Farid Hosseinizadeh†
Sharif University of Technology, 11365-8639 Tehran, Iran

This work deals with the popular topic of extending incompressible numerical formulations to the compressible or variable density regime. Based on an analogy between the incompressible and compressible governing equations, a general strategy is suitably developed to facilitate the compressible flow solution through using incompressible algorithms. It is shown that the implementation of the extended strategy to an arbitrarily incompressible algorithm requires two minor modifications in the original algorithm. In fact, two on/off switches suffice to implement the two required modifications. Switch one includes the compressible source terms to the momentum governing equations. Switch two decides how to calculate the unknown density field as a secondary dependent variable of the algorithm. In this work the two modifications are employed in a popular incompressible algorithm, which utilizes semi-implicit method with pressure-linked equation. However, one important advantage of the extended strategy is its robust applicability to the other constant density algorithms as well. The strategy is examined by testing a number of test cases at various Mach and Reynolds numbers. Results are presented for driven-cavity flow, flow over a backward-facing step, flow through a channel, and inviscid flow through a converging-diverging nozzle. The study shows that the modified algorithm exhibits similar performance for both constant and variable density regimes.

Nomenclature

e = internal energy
F, G = undetermined dependent variables
f, g = x- and y-momentum components; ρu and ρv
H = channel height
h = enthalpy
k = thermal conductivity coefficient
M = Mach number
P = dependent variable
p = pressure
R = gas constant
Re = Reynolds number
S = control volume face
s = source term
t = temperature
u, v = velocity components
x, y = coordinates directions
μ = viscosity
ν = kinematics viscosity
ρ = density
τ = stress tensor components

Superscripts

$+$ = nondimensionalized parameter
$-$ = lagged from previous iteration
$*$ = approximate magnitude
$'$ = correction magnitude

Introduction

PROGRESS in computational fluid dynamics and heat-transfer techniques has prompted researchers to develop incompressible algorithms capable of computing variable density fields. Today, the engineering problem requires the use of a single flow algorithm capable of targeting the broadest range of flow applications. For example, there are many practical problems in heat-transfer engineering where code developers desire to extend their incompressible procedure in order to take into account compressibility. Essentially, computational-fluid-dynamics workers categorize computational flow solvers into two basic categories of incompressible and compressible methods. The major parameter that creates such a classification is the implicit role of pressure in the continuity equation. This role vanishes in the incompressible limit. The artificial compressibility has been used as a primitive remedy to surmount this weak role.[1,2] The differences between incompressible and compressible procedures have encouraged researchers to investigate and develop unique algorithms capable of solving the both categories. For example, there has been a general interest in extending the SIMPLE-based calculation procedure[3] to compressible flow applications. As is known, the SIMPLE is employed on a staggered grid arrangement. In this regard velocities and pressure are derived in a segregated manner by solving the momentum equations and a pressure equation, respectively. Because the latter equation in its original form exhibits elliptic behavior, it cannot mimic the hyperbolic nature of highly compressible flow. This is a major difficulty in extending the SIMPLE to compressible flow applications.

There are several major works that extend the SIMPLE-based procedures to compressible flow applications. Van Doormaal et al.[4] compare several variants of the SIMPLE procedure for the solution of compressible flow using appropriate modification on the pressure equation. Karki and Patankar[5] employ the primitive idea of Patankar[3] and consider the compressible aspects of the flow in the original SIMPLE procedure using first-order upwinding. Shyy et al.[6] use a second-order upwinding to discretize the convective terms within a multigrid context. Marchi and Maliska[7] use an upwind scheme to treat density, convection, and convection-type terms. However, Demirdzic et al.[8] use a combination of central and upwind schemes to treat the preceding terms on a curvilinear coordinate system with variable base vectors. Greyvenstein and Meyer[9] use a mixed-differencing scheme for the convective terms in the momentum equation and a central differencing scheme for densities in the continuity equation and improve the accuracy of the SIMPLE method. As was mentioned earlier, the essence of the modification in these references is the primitive idea of Ref. 3, which considers an active role of density in the mass conservation expression. Similarly, Lien and Leschziner[10] employ a streamwise-directed

---

Received 29 July 2002; revision received 5 March 2003; accepted for publication 5 March 2003.

*Assistant Professor, Head of Aerodynamics and Propulsion Divisions, Department of Aerospace Engineering; darbandi@sharif.edu.

†Graduate Research Assistant, Department of Aerospace Engineering.

density-retardation concept in their collocated algorithm. Kobayashi and Pereira[11] incorporate an essentially nonoscillatory scheme[12] into a pressure-correction framework. Issa and Javareshkian[13] use a total-variation-diminishing scheme in their pressure-based algorithm. Date[14] similarly employs the idea of Ref. 3 and predicts the compressible solution by introducing a smoothing pressure correction concept. In a recent work Moukalled and Darwish[15] employ normalized variable formulation methodology to discretize the convection terms and use high-resolution schemes to interpolate density in mass fluxes.

The challenge of extending incompressible methods to compressible flow solutions and vice versa has been examined in the non-SIMPLE procedures as well. In a fully implicit control-volume-based finite element approach, Darbandi and Schneider[16] present an analogy between compressible and incompressible governing equations, which facilitates the extension of incompressible solvers to compressible flow applications. The analogy is developed on a collocated grid arrangement. The investigation shows excellent performance of a unified algorithm capable of solving both flow cases. Because the analogy is general, it is expected to be applicable to other incompressible flow algorithms as well. As a preliminary step toward generalizing the analogy, Ref. 17 explores the applicability of the analogy to the SIMPLE-based incompressible procedures. In this work the formulation presented in the preceding reference is suitably improved in order to minimize the required modifications for extending a dual-purpose algorithm. It is shown that the modification needs two simple steps. Step one implements the role of the extra part of compressible governing equations. Meanwhile, step two considers the type of density treatment in the algorithm. To demonstrate the performance of the extended strategy, the modified algorithm is eventually tested for solving the driven-cavity and the backward-facing step benchmark problems. The entry flow and the converging-diverging nozzle flow are also examined as additional test cases.

Governing Equations

If the fluid is assumed to be Newtonian and to obey Stokes' law, the two-dimensional steady-state Cartesian form of the governing equations is given by

$$\frac{\partial \mathcal{F}(\psi)}{\partial x} + \frac{\partial \mathcal{G}(\psi)}{\partial y} = \frac{\partial \mathcal{R}(\psi)}{\partial x} + \frac{\partial \mathcal{T}(\psi)}{\partial y} \tag{1}$$

where $\psi = (\{\rho\}, \rho u, \rho v, \rho e)^T$. The convection and diffusion flux vectors are written as

$$\mathcal{F} = (\rho u, \rho u^2 + p, \rho u v, \rho u h)^T \tag{2a}$$

$$\mathcal{G} = (\rho v, \rho v u, \rho v^2 + p, \rho v h)^T \tag{2b}$$

$$\mathcal{R} = (0, \tau_{xx}, \tau_{xy}, \sigma_x)^T \tag{3a}$$

$$\mathcal{T} = (0, \tau_{yx}, \tau_{yy}, \sigma_y)^T \tag{3b}$$

The energy dissipation terms are $\sigma_x = u\tau_{xx} + v\tau_{xy} - q_x$ and $\sigma_y = u\tau_{yx} + v\tau_{yy} - q_y$. The stress tensor components are given by

$$\tau_{xx} = 2\mu\frac{\partial u}{\partial x} - \left\{\frac{2}{3}\mu\left(\frac{\partial u}{\partial x} + \frac{\partial v}{\partial y}\right)\right\} \tag{4a}$$

$$\tau_{yy} = 2\mu\frac{\partial v}{\partial y} - \left\{\frac{2}{3}\mu\left(\frac{\partial u}{\partial x} + \frac{\partial v}{\partial y}\right)\right\} \tag{4b}$$

$$\tau_{xy} = \tau_{yx} = \mu\left(\frac{\partial u}{\partial y} + \frac{\partial v}{\partial x}\right) \tag{4c}$$

The components of the heat flux are given by $q_x = -k\partial t/\partial x$ and $q_y = -k\partial t/\partial y$. The perfect gas law is used to close the preceding system of equations, that is, $p = \rho R t$. Alternatively, for the incompressible flow case the equation of state can be written as $\rho = \text{constant}$. The terms inside braces { } vanish in the incompressible limit resulting in a new form for the governing equations.

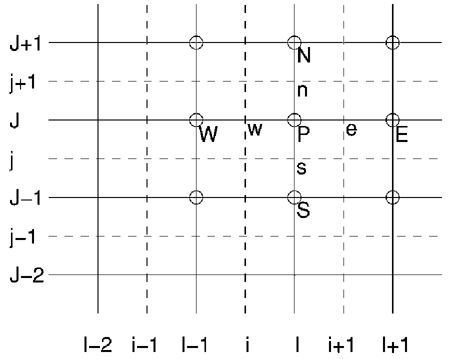

Fig. 1 Staggered-based domain discretization and nomenclature.

Domain Discretization

The two-dimensional solution domain is discretized in a staggered grid manner. It means that the domain is divided into a number of quadrilateral control volumes which do not overlap each other and fully cover the solution domain (see Fig. 1). In this arrangement nodes are located at the center of control volumes and are the locations of pressure field computation. They are shown by circles in Fig. 1 and labeled by upper-case letters such as P, E, W, N, and S. However, velocities are computed at the cell faces. These faces are labeled by lower case letters such as e, w, n, and s. This dual-grid considerations for the dependent variable computation on two adjacent grids is known as the staggered grid arrangement.[3] To simplify the notations in the Computational Modeling section, we use capital letter subscripts of I and J to enumerate the main grid lines that pass nodal points in x and y directions, respectively, and lower-case subscripts of i and j to enumerate the grid lines that pass cell faces in the x and y directions, respectively.

Computational Modeling

To extend a dual-purpose unified algorithm, the integration of a suitable re-arrangement of the governing equations over an arbitrary control volume yields

$$\int_S (F\boldsymbol{i} + G\boldsymbol{j}) \cdot \mathrm{d}\boldsymbol{S} = 0 \tag{5}$$

$$\int_S \left[(u)F\boldsymbol{i} + (v)F\boldsymbol{j} + P\boldsymbol{i} - \nu\frac{\partial F}{\partial x}\boldsymbol{i} - \nu\frac{\partial F}{\partial y}\boldsymbol{j}\right] \cdot \mathrm{d}\boldsymbol{S} = \bar{s}^x \tag{6}$$

$$\int_S \left[(u)G\,\boldsymbol{i} + (v)G\boldsymbol{j} + P\boldsymbol{j} - \nu\frac{\partial G}{\partial x}\boldsymbol{i} - \nu\frac{\partial G}{\partial y}\boldsymbol{j}\right] \cdot \mathrm{d}\boldsymbol{S} = \bar{s}^y \tag{7}$$

The integration over cell faces is indicated by S. In addition, $\mathrm{d}\boldsymbol{S}$ is an outward vector normal to the cell faces. The upper-case letters of F, G, and P have been chosen as the undetermined dependent variables of the solution algorithm. They are left to be explained later. However, at this stage one can simply assume them as $F = \rho u$, $G = \rho v$, and $P = p$. All other velocity parameters in the parenthesis are the nonlinear parts of the equations, which in turn need to be linearized. In the SIMPLE-based procedures the other transport equations, such as the energy equation, are treated separately after a segregate solution of the continuity and momentum equations. This is why the energy equation is not observed in Eqs. (5–7).

The $\bar{s}^x$ and $\bar{s}^y$ are source terms, which consist of two parts. First, they include the additional diffusion terms in the compressible equations, that is, the terms inside braces in Eq. (4). Second, they include the terms that are produced after linearizing the nonlinear diffusion terms with respect to the chosen dependent variables. Following Ref. 17, the latter linearization for nonlinear $\mu(\partial u/\partial x)$ and $\mu(\partial u/\partial y)$ terms with respect to $F = \rho u$ yields

$$\mu\frac{\partial u}{\partial x} = \nu\frac{\partial F}{\partial x} - \nu u\frac{\partial \rho}{\partial x} \tag{8}$$

$$\mu\frac{\partial u}{\partial y} = \nu\frac{\partial F}{\partial y} - \nu u\frac{\partial \rho}{\partial y} \tag{9}$$

As is seen, the preceding linearizations produce additional nonlinear density gradients. The transfer of such density gradients into $\bar{s}^x$ and $\bar{s}^y$ terms finally yields

$$\begin{aligned}\bar{s}^x = {} & \int_S \frac{\mu}{3}\left\{\left(\frac{\partial u}{\partial x} - 2\frac{\partial v}{\partial y}\right)\boldsymbol{i} + 3\frac{\partial v}{\partial x}\boldsymbol{j}\right\}\cdot \mathrm{d}\boldsymbol{S} \\ & - \int_S \mu\frac{u}{\rho}\left(\frac{\partial \rho}{\partial x}\boldsymbol{i} + \frac{\partial \rho}{\partial y}\boldsymbol{j}\right)\cdot \mathrm{d}\boldsymbol{S}\end{aligned} \tag{10}$$

$$\begin{aligned}\bar{s}^y = {} & \int_S \frac{\mu}{3}\left\{3\frac{\partial u}{\partial y}\boldsymbol{i} + \left(\frac{\partial v}{\partial y} - 2\frac{\partial u}{\partial x}\right)\boldsymbol{j}\right\}\cdot \mathrm{d}\boldsymbol{S} \\ & - \int_S \mu\frac{v}{\rho}\left(\frac{\partial \rho}{\partial x}\boldsymbol{i} + \frac{\partial \rho}{\partial y}\boldsymbol{j}\right)\cdot \mathrm{d}\boldsymbol{S}\end{aligned} \tag{11}$$

As is observed, the first integrations represent additional diffusion terms in the compressible equations. However, the second integrations are additional density gradients generated after linearizing the nonlinear incompressible diffusion terms. The bar over $\bar{s}$ means it is explicitly estimated from the known values of the last iteration. As is expected, these source terms vanish in the incompressible limit. Indeed, if the source terms are explicitly calculated from the latest magnitudes of the variables they do not need any further linearizations. However, we once more linearize the velocity gradient terms with respect to the chosen dependent variables in order to achieve some advantages. The additional linearization, similar to those in Eqs. (8) and (9), of the velocity gradients in Eqs. (10) and (11) finally results in

$$\begin{aligned}\bar{s}^x = {} & \int_S \frac{\nu}{3}\left[\left(\frac{\partial F}{\partial x} - 2\frac{\partial G}{\partial y}\right)\boldsymbol{i} + 3\frac{\partial G}{\partial x}\boldsymbol{j}\right]\cdot \mathrm{d}\boldsymbol{S} \\ & - \int_S \frac{\nu}{3}\left[\left(4\frac{F}{\rho}\frac{\partial \rho}{\partial x} - 2\frac{G}{\rho}\frac{\partial \rho}{\partial y}\right)\boldsymbol{i} - 3\left(\frac{G}{\rho}\frac{\partial \rho}{\partial x} + \frac{F}{\rho}\frac{\partial \rho}{\partial y}\right)\boldsymbol{j}\right]\cdot \mathrm{d}\boldsymbol{S}\end{aligned} \tag{12}$$

$$\begin{aligned}\bar{s}^y = {} & \int_S \frac{\nu}{3}\left[3\frac{\partial F}{\partial y}\boldsymbol{i} + \left(\frac{\partial G}{\partial y} - 2\frac{\partial F}{\partial x}\right)\boldsymbol{j}\right]\cdot \mathrm{d}\boldsymbol{S} \\ & - \int_S \frac{\nu}{3}\left[3\left(\frac{F}{\rho}\frac{\partial \rho}{\partial y} + \frac{G}{\rho}\frac{\partial \rho}{\partial x}\right)\boldsymbol{i} + \left(-2\frac{F}{\rho}\frac{\partial \rho}{\partial x} + 4\frac{G}{\rho}\frac{\partial \rho}{\partial y}\right)\boldsymbol{j}\right]\cdot \mathrm{d}\boldsymbol{S}\end{aligned} \tag{13}$$

Versteeg and Malalasekera[18] show that the proper treatment of the incompressible form of Eqs. (6) and (7) results in two sets of algebraic equations, which can be separately solved to estimate approximate u, that is, u^*, and v, that is, v^*, velocity fields. In this case both source terms are zero, and the two equations are simplified by extracting density from F and G dependent variables. Eventually, the two sets of algebraic equations are written as

$$a_{i,J}u^*_{i,J} = \sum a_{\mathrm{nb}}u^*_{\mathrm{nb}} + \left(p^*_{I-1,J} - p^*_{I,J}\right)A_{i,J} + b_{i,J} \tag{14}$$

$$a_{I,j}v^*_{I,j} = \sum a_{\mathrm{nb}}v^*_{\mathrm{nb}} + \left(p^*_{I,J-1} - p^*_{I,J}\right)A_{I,j} + b_{I,j} \tag{15}$$

where $A_{i,J}$ and $A_{I,j}$ are the cell face areas at east (or west) and south (or north) of the u-control volume, respectively. Similarly, $b_{i,J}$ and $b_{I,j}$ indicate the source terms in the x- and y-momentum equations, respectively. The values of the coefficients $a_{i,J}$, $a_{I,j}$, $b_{i,J}$, $b_{I,j}$, and a_{nb} are determined after choosing a proper choice for convection-diffusion model such as upwind, hybrid, QUICK, etc. schemes. All velocity components that appear in the preceding coefficients are lagged. In the preceding equations, if a pressure field, say p^*, is guessed the system of equations can be solved for the subsequent velocity components, that is, u^* and v^*. In fact, this strategy is a guess-and-correct tactic, which is entirely analogous to an algorithm named SIMPLE (Semi-Implicit Method for Pressure-Linked Equations).[3] The question is how we can properly guess the pressure field.

An analogous treatment of general form of Eqs. (6) and (7) results in two sets of algebraic equations, which can be separately solved to estimate the approximate value of F^* and G^* unknowns.[17] They are derived from

$$a_{i,J}F^*_{i,J} = \sum a_{\mathrm{nb}}F^*_{\mathrm{nb}} + \left(P^*_{I-1,J} - P^*_{I,J}\right)A_{i,J} + b_{i,J} + \alpha\bar{s}^x_{i,J} \tag{16}$$

$$a_{I,j}G^*_{I,j} = \sum a_{\mathrm{nb}}G^*_{\mathrm{nb}} + \left(P^*_{I,J-1} - P^*_{I,J}\right)A_{I,j} + b_{I,j} + \alpha\bar{s}^y_{I,j} \tag{17}$$

The role of parameter α is explained shortly. It must be defined in a manner that removes the role of compressibility in the incompressible condition.

Although the incompressible continuity equation does not involve any pressure term, it can be used as a complementary equation to obtain a better estimate or prediction of the pressure field. Reference 18 shows that the continuity equation can be converted to a pressure-correction equation. We similarly develop a pressure-correction equation in terms of the selected P variable. This equation is given by

$$\begin{aligned}a_{I,J}P'_{I,J} = {} & a_{I+1,J}P'_{I+1,J} + a_{I-1,J}P'_{I-1,J} + a_{I,J+1}P'_{I,J+1} \\ & + a_{I,J-1}P'_{I,J-1} + b_{I,J}\end{aligned} \tag{18}$$

where $a_{I,J} = a_{I+1,J} + a_{I-1,J} + a_{I,J+1} + a_{I,J-1}$. The primes indicate the required corrections to correct the stars. This equation provides a tool to estimate the pressure correction field $P'_{I,J}$ at all nodal grid points. In the SIMPLE algorithm Eqs. (14) and (15) are first used to compute u^* and v^*. Then, the pressure-correction magnitude is used to correct the preceding approximate pressure and velocity values. We similarly use Eqs. (16) and (17) to obtain F^* and G^*. Next, the pressure-correction magnitude is used to correct the preceding approximate values of the dependent variables. The correction yields

$$P = P^* + P' \tag{19}$$

$$F_{i,J} = F^*_{i,J} + d_{i,J}(P'_{I-1,J} - P'_{I,J}) \tag{20}$$

$$G_{I,j} = G^*_{I,j} + d_{I,j}(P'_{I,J-1} - P'_{I,J}) \tag{21}$$

where $d_{i,J} = A_{i,J}/a_{i,J}$ and $d_{I,j} = A_{I,j}/a_{I,j}$.

The rest of the SIMPLE procedure is to solve the other discretized transport equations such as energy and to update the secondary dependent variables such as nonconstant fluid properties. For example, if the density field is treated as a secondary dependent variable it needs to be updated right at this stage. By the end of this procedure, this iteration is completed. However, if the residuals are not low enough at the end of this iteration the procedure is repeated for the next iteration. Using the outcomes of the last iteration, the inputs to the next iteration are approximated by

$$P^* = P, \qquad F^* = F, \qquad G^* = G \tag{22}$$

As is observed, the procedure in our extended algorithm consists of solving the three systems of algebraic equations given by Eqs. (16–18), correcting the approximate magnitudes of dependent variables through Eqs. (19–21), and updating the dependent variables for the next iteration, Eq. (22). This procedure is independent of the choice of incompressible or compressible considerations. This suggests that the two compressible and incompressible algorithms are essentially the same except for the magnitudes of the extra source terms in the right-hand side of Eqs. (6) and (7). If we consider a switch for including and excluding these two source terms in the formulations, we will take one step toward unifying the two algorithms. In this regard switch one is defined as

$$\text{Switch One}\begin{cases}\text{OFF} & \alpha = 0 \quad \text{incompressible} \\ \text{ON} & \alpha = 1 \quad \text{compressible}\end{cases} \tag{23}$$

Indeed, the $\bar{s}^x$ and $\bar{s}^y$ automatically vanish in the incompressible limit and do not normally need the preceding consideration. However, the numerical treatment of these two terms results in truncation and round-off errors, which can in turn boost up the differences between the results of two algorithms in the incompressible limit. Therefore, the employment of this switch to the source terms is only for caution.

One more consideration is needed to unify the two algorithms completely. As was mentioned earlier, if we consider density as a secondary variable it is needed to be updated at the end of each iteration. The density treatment needs special care in our compressible algorithm. Therefore, we define switch two in order to determine the two types of density treatments in a single algorithm. This switch is set as

$$\text{Switch Two}\begin{cases}\text{OFF} & \rho = \text{constant} = \rho_0 \\ \text{ON} & \rho = p/Rt\end{cases} \tag{24}$$

where the preceding equation of state is valid for a calorically perfect gas.

The addition of these two switches and the two source terms into an arbitrary incompressible algorithm enables it to solve both compressible and incompressible flows. The key point in this extension is the critical role of the chosen dependent variables. The chosen dependent variables guarantee their dual roles in a unified algorithm. A suitable choice of dependent variables can be written as

$$\{F, G, P\} = \begin{cases}\{u, v, p/\rho_0\} & \text{incompressible} \\ \{\rho u, \rho v, p\} & \text{compressible}\end{cases} \tag{25}$$

The p/ρ_0 division only multiplies the magnitude of the real pressure field by a constant factor of $1/\rho_0$ with no side effects on the magnitude of u- and v-velocity fields. The investigation of the new extended formulation shows that we can arbitrarily substitute u, v, and p/ρ_0 with ρu, ρv, and p without declining the performance of either incompressible or compressible parts. Indeed, the set of modified equations works equally for both choices of the dependent variables. On the other hand, since the velocity components do not appear in the compressible source terms we do not need to calculate velocities when we use the undetermined dependent variables in our algorithm. In another words, we do not change anything in the incompressible algorithm except adding two on/off switches and calculating two additional source terms. To obtain a compressible solution, both switches must be turned on; otherwise, both of them must be off.

Results and Discussion

In this section the extended strategy is tested for solving a number of test problems. Before presenting the compressible and incompressible results and comparing them with each other, it is essential to determine the accuracy of the chosen method. As was discussed in the preceding section, the chosen method is a semi-implicit control-volume method with pressure-linked equation known as SIMPLE. In the current work we do not intend either to focus on developing the SIMPLE or validating its accuracy. These topics are essentially known for many computational-fluid-dynamics (CFD) workers and have been reported in CFD books.[3,18] Here, we would like to illustrate the performance of a dual-purpose computational algorithm, which is used as either a compressible or an incompressible flow solver. In another words, we want to illustrate the performance of our extended strategy, which enables an existing incompressible method to take into account the density variation in low Mach number and subsonic flow regimes.

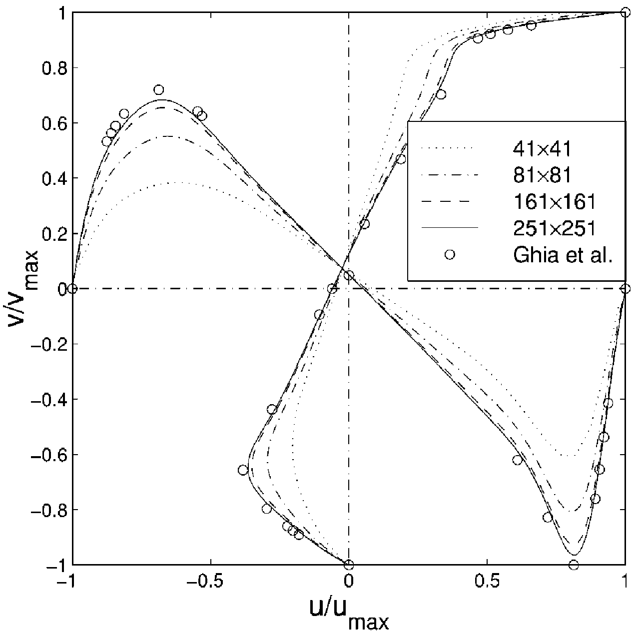

Fig. 2 Results of grid refinement study in cavity and comparison with benchmark solution.

The first test case problem is a two-dimensional square cavity driven by the movement of its lid. This model is isothermally tested at two different Reynolds numbers of 10^3 and 3.2×10^3 using uniform grid distributions of 41×41, 81×81, 161×161, and 251×251. The last grid resolution provides grid-independence solutions at $Re = 10^3$ and 3.2×10^3. The cavity has a unit length scale. All velocities are nondimensionalized by the lid velocity magnitude.

As was mentioned earlier, although the accuracy of the selected method is an irrelevant topic in the current study, Fig. 2 demonstrates the centerline velocities for four different grid distributions and compares them with the benchmark solution.[19] The Reynolds number is 10^3, and the flow is incompressible. The u-velocity and v-velocity distributions are plotted along vertical and horizontal centerlines, respectively. As is observed, a grid resolution of 251×251 is relatively suitable to show the grid-independent solution. The agreement between the fine grid and benchmark solutions is good; however, it can be improved by using better flux interpolators at the cell faces.

In the next stage the incompressible result of cavity is compared with the results of three different compressible flow cases of $M = 0.001$, 0.3, and 0.7. Figures 3 and 4 present the centerline velocity distributions at $Re = 10^3$ and 3.2×10^3, respectively. As is observed, both the incompressible and the compressible solutions perform almost identical velocity profile at each Reynolds number. This independence of solution to Mach number in the cavity problem is also reported by other references.[16,20]

Figure 5 demonstrates the convergence history of the algorithm at $Re = 10^3$ and 3.2×10^3. The key point in this figure is the identical exhibition of the convergence behavior at each Reynolds number. Such identical performances are not normally performed by many other compressible flow algorithms or solvers.[21] Pletcher and Chen[20] also solve the cavity problem at $Re = 100$ for a wide range of Mach numbers using a grid distribution of 19×19. They show that the number of iterations drastically increases as flow Mach number decreases. In their work the number of iterations increases from 138 to 2123 as the Mach number decreases from 0.2 to 0.002. Similarly, Ajmani et al.[22] show that the number of iterations remarkably increases if no special treatment is employed in their compressible algorithm in order to solve low compressible models. As is observed in Fig. 5, the convergence behavior starts deviating from the incompressible one at higher Mach numbers. It is because a higher compressibility raises the magnitudes of the source terms in the right-hand side of Eqs. (6) and (7). Because the SIMPLE algorithm

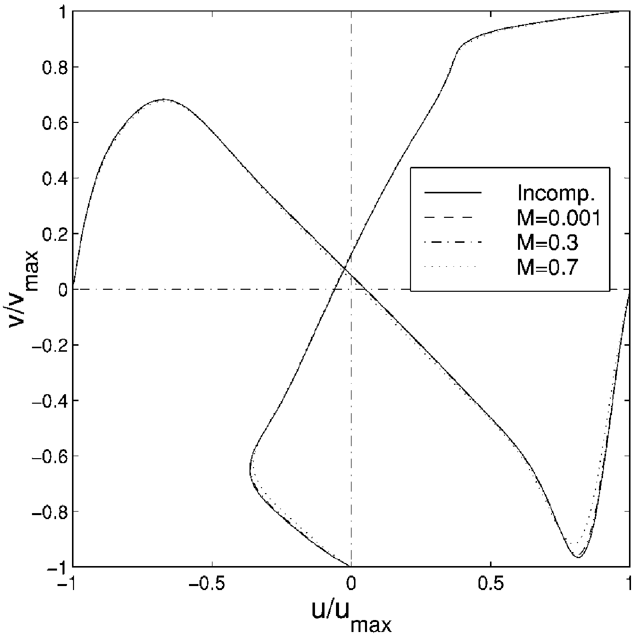

Fig. 3 Comparative study of centerline velocity profiles in cavity; $Re = 10^3$ and grid 251 × 251.

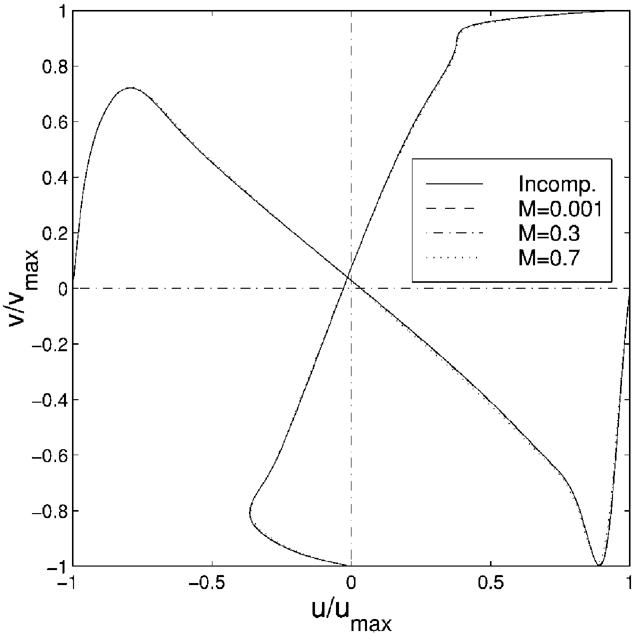

Fig. 4 A comparative study of centerline velocity profiles in cavity; $Re = 3.2 \times 10^3$ and grid 251 × 251.

highly depends on the magnitude of the underrelaxation parameter, a constant performance for different compressible cases might not be achieved unless this parameter is appropriately decreased. In the current work the workers consider almost fixed underrelaxation magnitude for each test case. This consideration restricts the upper limit of flow Mach number.

The second test problem is a backward-facing step flow. The geometry and flow considerations are identical with those of Gartling[23] and Pepper et al.[24] Considering a total channel height of H, the step height and downstream channel length are $H/2$ and $30H$, respectively. The flow boundary conditions for the step geometry include the no-slip velocity specifications for all solid surfaces, a parabolic velocity profile at the inlet $U(y) = 1.5 \times U_{\text{mean}}(4y^+)(2 - 4y^+)$, where $0 \le y^+ (= y/H) \le 0.5$, and both zero normal stress and uniform pressure distribution at the outflow. Following Pepper et al.[24] the back of the step is taken as adiabatic, and a constant heat flux out of $q_w = 9.6$ per unit length is considered for the upper and lower walls. The nondimensional temperature profile at the inflow is given by $t(y) = [1 - (4y^+ - 1)^2][1 - (4y^+ - 1)^2/5]$, where $0 \le y^+ \le 0.5$. At the outflow boundary the temperature distribution is extrapolated from the interior nodes. The problem is tested for a broad range of Reynolds numbers of which the results for three Reynolds numbers of 4×10^2, 6×10^2, and 8×10^2 are presented in here. The grid is uniformly distributed in x and y directions. Solutions were obtained for different grid densities to ensure solution accuracy. The investigation shows that a grid resolution of 600 × 50 is fine enough to produce a grid-independence solution at the preceding Reynolds numbers. Therefore, we use this grid resolution to present the current results.

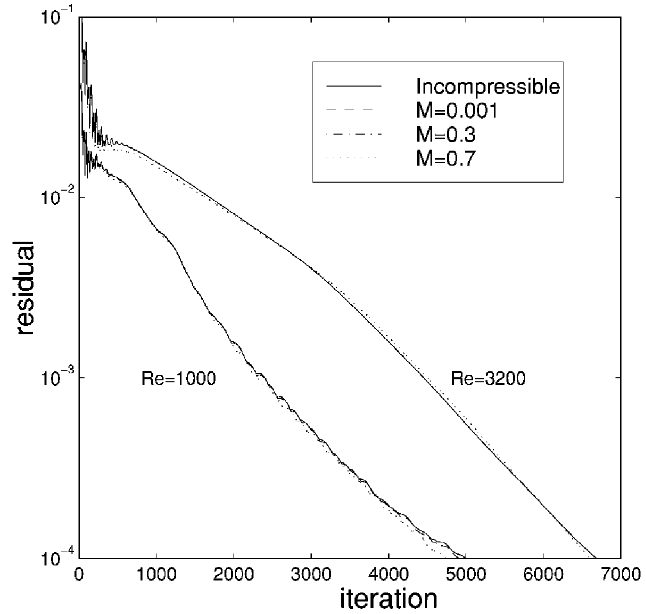

Fig. 5 Comparison of convergence histories for cavity using different Mach- and Reynolds-number values.

At this stage the authors would like to raise one important point on the role of momentum component f in the following test cases, which involve inflow and outflow boundary conditions. In these tests we normally use f profiles instead of u profiles to demonstrate the results. This choice helps us to provide identical boundary conditions at the inlet for both compressible and incompressible cases. If we specify velocity at the inlet, we are not able to specify $f = \rho u$ in there because we have no control on the density magnitude. In fact, the inlet density is calculated via the equation of state. Because the inlet pressure is not known, the inlet density is also unknown. To fix the inlet Reynolds number for different compressible flow cases, that is, different Mach numbers, we specify f instead of u at the sinlet. Fortunately, because the momentum component is a part of the Reynolds-number definition we can fix the Reynolds number for the incompressible and the subsequent compressible flow cases. Unfortunately, contrary to the Reynolds number, the inlet Mach number cannot be specified at the inlet using this strategy. Therefore, in the following results, whenever we talk about the Mach number it is the magnitude of maximum Mach number in the solution domain that is not necessarily located at the inlet. The benefits of this strategy are shown shortly in the following figures.

Figure 6 shows the axial momentum component profiles at different longitudinal locations of the channel at Reynolds of 4×10^2 and 6×10^2. It depicts the qualitative progress of the f profiles at six locations of $x^+ = x/H = 1.5$, 3.0, 5.0, 7.0, 15.0, and 29.5. Linear interpolation has been used to derive the results from the computed values at the nearest nodes for the specified locations. At this stage we are not concerned with the details of the solution. However, we are essentially interested in the performance of the extended algorithm that is able to include the density variation in an incompressible algorithm. The results are given for both incompressible and

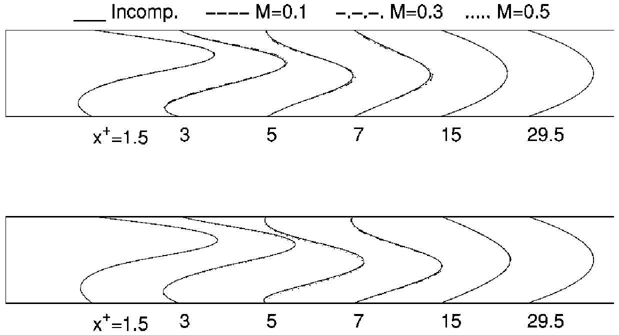

Fig. 6 Typical *f* profiles at different locations in a backward-facing step channel; $Re = 4 \times 10^2$ (top) and 6×10^2 (bottom), grid 600 × 50.

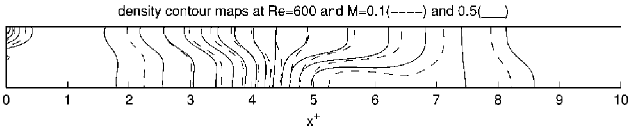

Fig. 7 Density contours in a backward-facing step channel at $Re = 6 \times 10^2$ and $M = 0.1$ and 0.5.

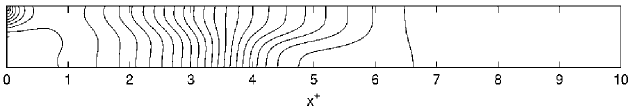

a) $Re = 4 \times 10^2$

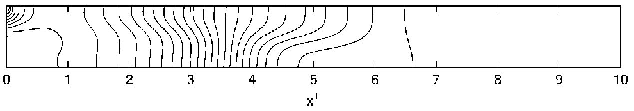

b) $Re = 6 \times 10^2$

Fig. 8 Density contours in a backward-facing step channel at $M = 0.5$ using $Re = 4 \times 10^2$ and 600.

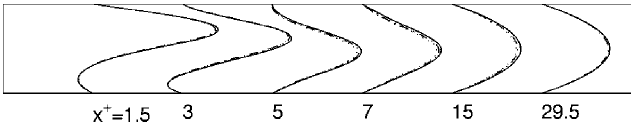

Fig. 9 Typical *u* profiles at different locations in a backward-facing step channel; $Re = 4 \times 10^2$ and grid 600 × 50.

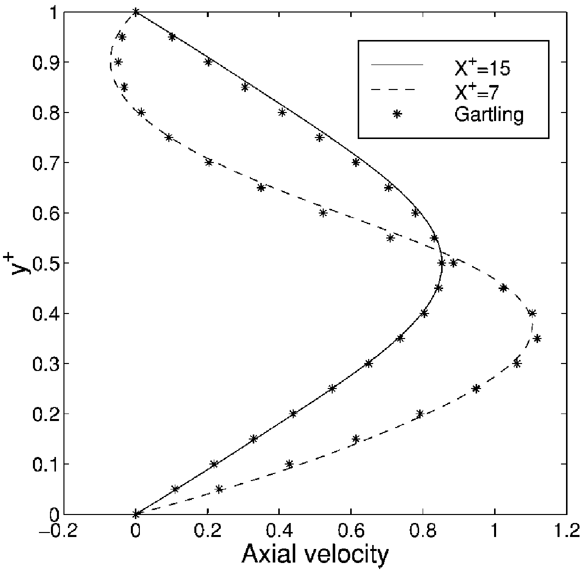

Fig. 10 Comparative study in the backward-facing step channel at $Re = 800$, grid 600 × 50.

compressible flow conditions using three different Mach numbers of $M = 0.1$, 0.3, and 0.5. The reported Mach numbers are the highest magnitude of Mach number in the channel at each flow case. As was discussed in the cavity problem, the upper limit of Mach number is determined by considering identical convergence behavior for both compressible and incompressible cases. The figure shows that the magnitude of f is negative close to the step wall because of the recirculating zone. However, the flow slowly recovers toward a fully developed Poiseuille flow near the exit of the channel. In addition, there is a secondary recirculation zone attached to the upper wall beginning near the reattachment point of the lower eddy. The existence of this secondary vorticity totally depends on the flow Reynolds number. Indeed, the upper eddy rapidly vanishes as the Reynolds number decreases. Figure 6 also shows that the results of incompressible and compressible flow cases are close at each specific Reynolds number.

To illustrate the density distribution in the compressible domain, Fig. 7 presents contour plots of density at $Re = 6 \times 10^2$ and two Mach numbers of 0.1 and 0.5. As is observed, the density field is almost invariant. It is because the density field mimics the pressure field, which is almost invariant for the preceding flow conditions. The results of a similar study for a fixed Mach number and two different Reynolds numbers are illustrated in Fig. 8. The figure represents the results at $M = 0.5$ while the Reynolds number is 4×10^2 (Fig. 8a) and 6×10^2 (Fig. 8b). The investigation shows that the density contour plots are similar to pressure contour plots.

Figure 9 plots the schematic u profiles in the solution domain at $Re = 4 \times 10^2$. Comparing with Fig. 6, the velocity profiles are very similar to the momentum component profiles, at least at this Reynolds number. However, the study shows that as the Reynolds number decreases the density variation increases. For the sake of brevity, this effect will be discussed more in the third test problem, which performs higher density variation.

Unfortunately, to the knowledge of the current authors, there is no archival results for the compressible backward-facing step flow except for very low Mach numbers, for example, Ref. 2. However, there are several incompressible benchmark solutions that can be used for validating the current results. Figure 10 compares the current solution with that of Gartling[23] at $Re = 8 \times 10^2$. Following Gartling, the comparisons are presented at two different longitudinal locations of $x^+ = x/H = 7.0$ and 15.0. The results at $x^+ = 7.0$ indicate the existence of a strong eddy near the upper wall. Despite performing good agreement with the benchmark solution, once more, we would like to mention that the main objective of this work is not to improve the accuracy of the chosen method. The primary interest has been to show the performance of our dual-purpose algorithm.

Besides the benchmark works in the fluid flow part, there is a number of benchmarks that study the heat-transfer phenomenon in the solution domain. Figure 11 depicts the temperature distributions along the upper and lower walls of the channel at $Re = 8 \times 10^2$. As is seen, the temperature on the lower wall initially increases until the reattachment point and then decreases along the channel. This behavior is similarly observed at the other Reynolds numbers. Similarly, the upper eddy causes a steep gradient in temperature profile on the top wall including an abrupt decrease followed by an abrupt increase. Sufficiently downstream of the recirculation zones, fully developed flow conditions are approached with the temperature values themselves decreasing linearly with distance. The current results are compared with the numerical solution of Pepper et al.[24] with close agreement.

Figure 12 shows the isotherm distributions within the domain at $Re = 8 \times 10^2$. The domain has been broken into two parts to magnify the interior behavior. The effect of the recirculation zone on the temperature field is clearly observed in this figure. As is seen, the thermal boundary layer develops symmetrically beyond the top recirculation zone. The complex behavior of the temperature field in the domain can be observed by examining the temperature distributions on the top and bottom walls of the channel (Fig. 11).

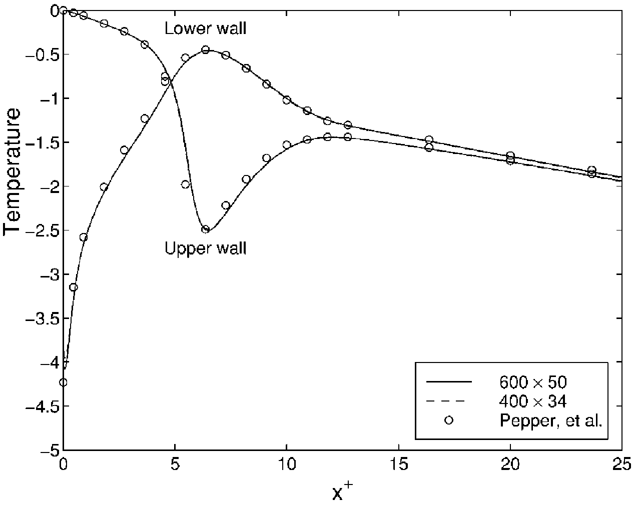

Fig. 11 Temperature distributions on the top and bottom walls of the backward-facing step channel at $Re = 8 \times 10^2$.

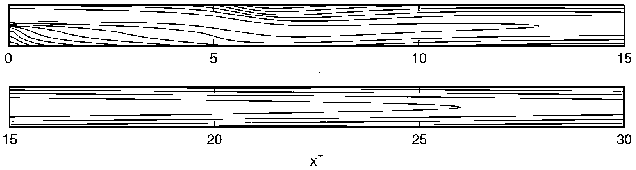

Fig. 12 Isotherms in the first (top) and second (bottom) halves of the backward-facing step domain, $Re = 8 \times 10^2$.

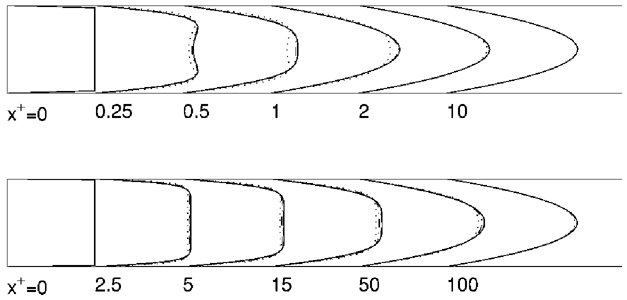

Fig. 13 Typical f profiles at different locations in a channel; $Re = 20$ (top) and 2×10^3 (bottom) using grid 210 × 40.

The third test problem is developing flow in a channel. The parallel plates duct geometry is a limiting geometry for the family of both rectangular and concentric annular ducts. There are a variety of approximate analytical and numerical methods for the determination of the flow characteristics on this region. The distance between two plates is $H = 1$. The x position is nondimensionalized by the channel height. The length of the solution domain is always longer than the predicted entrance length. For example, it is $5H$ at Reynolds 20 and $150H$ at Reynolds 2×10^3. The boundary condition implementation is very similar to that of backward-facing step except specifying a uniform f profile at the inlet. Reynolds numbers of 20 and 2×10^3 are chosen to present the results on uniform grids. To demonstrate the performance of the compressible part of the algorithm, Mach numbers of 0.001, 0.1, 0.3, and 0.5 are chosen. The choice of this upper limit for Mach was discussed in the cavity problem.

Typical f profiles are shown in Fig. 13 using $Re = 20$ and 2×10^3. As is expected, the qualitative developments of the profiles in compressible flow are similar to that of incompressible flow. As is seen, the profiles close to the entrance show a local minimum at the center of duct and symmetrically two maxima near the walls. The existence of these overshoots has been reported by other investigators as well.[25,26] It is because of an imposing uniform profile at the entry plane that forces a singularity in the wall pressure at the inlet. As is observed, the effect is the strongest at low Reynolds number and disappears as the Reynolds number approaches infinity. The thin-plate cascade entry problem that the boundary conditions imposed far upstream of the entry plane is an alternative that does not perform overshoots.

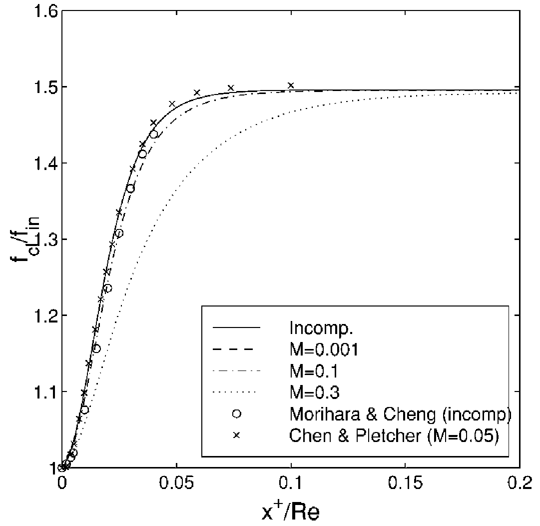

Fig. 14 Variation of the centerline f with axial distance in the entrance region of a channel; $Re = 20$ and grid 210 × 40.

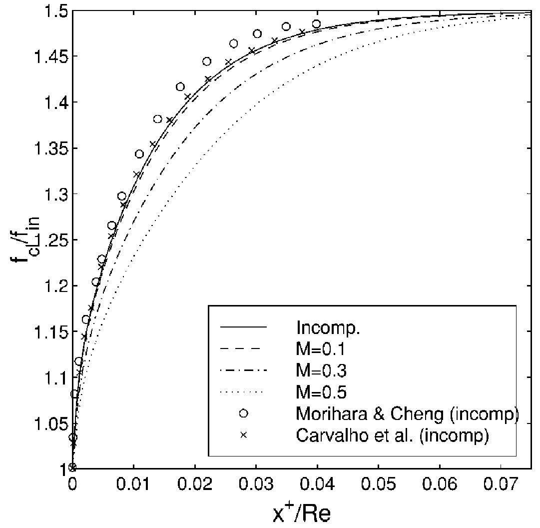

Fig. 15 Variation of the centerline f with axial distance in the entrance region of a channel; $Re = 2 \times 10^3$ and grid 210 × 40.

Figures 14 and 15 illustrate the distribution of the momentum component parameter at the centerline of the channel for both incompressible and different compressible cases. A uniform grid of 210×40 is used to obtain the results at $Re = 20$ and 2×10^3, with grid independence checked for centerline distributions through finer meshes at each Reynolds number. As is observed, the compressibility effect is negligible at lower Mach numbers. To validate the current results, they are compared with those of Morihara and Cheng,[25] who solve the quasilinear Navier–Stokes equations for incompressible flow; Carvalho et al.,[27] who use the integral transform method applicable to high-Reynolds-number flows, that is, $Re \to \infty$; and compressible results of Chen and Pletcher[28] at $M = 0.05$. Generally speaking, the agreement between the current results and those of others is excellent. As is seen, the centerline magnitudes decrease as Mach number increases. Schwartz[29] studies fully developed compressible flows in a channel for a range of subsonic Mach numbers using analytical perturbation techniques. He reports that the effect of Mach number is to flatten the velocity

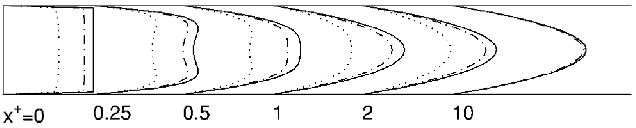

Fig. 16 Typical u profiles at different locations in a channel; $Re = 20$ and grid 210 × 40.

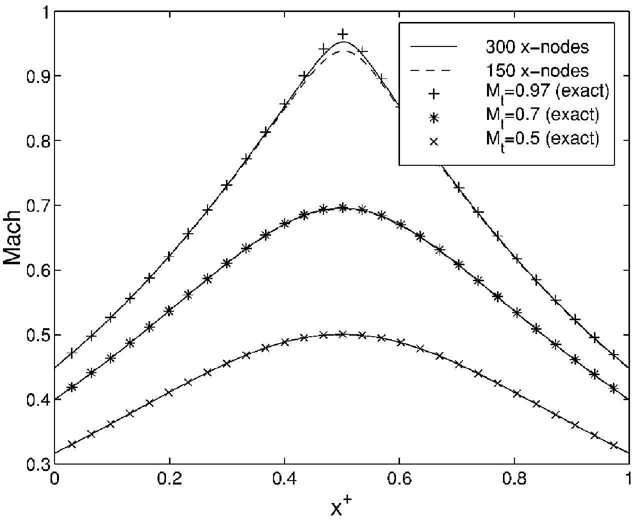

Fig. 17 Mach distribution along the centerline of a converging-diverging nozzle.

profile relative to the incompressible Poisseuille parabola. As is reported, the effect becomes more pronounced as Mach number approaches one.

Figure 16 illustrates the qualitative progress of the velocity profiles in the solution domain for different flow conditions at $Re = 20$. As was discussed, a variable density at the inlet does not permit the fixing of the Reynolds number at the inlet section if the flow is compressible. Contrary to Fig. 13, it shows that a suitable strategy to fix the Reynolds number is to specify f instead of u at the inlet section.

To present the performance of the extended strategy in solving the problems with a broad range of compressibility, the converging-diverging nozzle is chosen as the fourth test case. The geometry of the nozzle is given by $y(x) = 1 + (x - 1.5)^2/5$, where $0 \leq x \leq 3.0$. The grid nodes along the longitudinal direction are 150 and 300. Considering the inviscid flow condition, the current results can be compared with the exact solutions. The boundary conditions include specified uniform velocity at the inlet, inviscid walls, specified pressure at the outlet, specified temperature at the inlet, and adiabatic walls. The problem is examined at different low- and high-Mach-number regimes. To save the space, the results at the high-Mach-number regime are demonstrated and discussed in here. At the low-Mach-number regime the performance of the extended strategy is similar to those of the preceding test cases.

Figure 17 demonstrates the Mach distributions along the centerline of the nozzle. The results are shown for three different Mach numbers. The reported Mach numbers in this figure, that is, $M_t = 0.5$, 0.7, and 0.97, indicate the maximum Mach that is predicted by the exact solution at the throat of nozzle. The current results are compared with those of exact solution. As is observed, they are in good agreement with the exact solution considering different Mach ranges. However, there is slight difference between the two numerical and exact solutions at the vicinity of choking condition. It is caused by the high sensibility of the throat Mach number to the magnitude of the specified velocity at the inlet plane as the inlet boundary condition. Figure 18 similarly shows the temperature distributions along the centerline of the nozzle for the same specified Mach numbers at the throat.

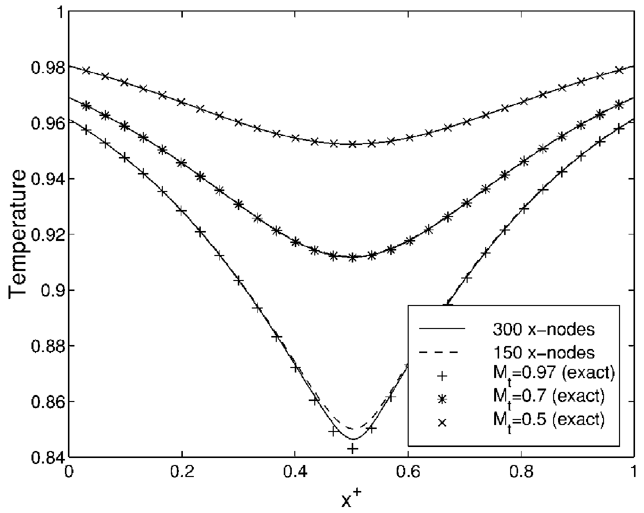

Fig. 18 Temperature distribution along the centerline of a converging-diverging nozzle.

Conclusion

The main objective of this work is to extend a dual-purpose algorithm by developing an arbitrarily incompressible algorithm using minimum possible modifications. In this regard an original semi-implicit method with pressure-linked equation, which solves incompressible flow on a staggered grid, is suitably developed for solving compressible flow. It is shown that a suitable choice of dependent variables ensures smooth transition from incompressible to compressible flow solutions. In fact, the employment of the momentum components as an alternative to the velocity components minimizes the required modifications. The primary interest in this study has been to show the performance of the extended dual-purpose algorithm. Therefore, we show that the extended algorithm works identically for solving both compressible and incompressible flow regimes. In this regard several test problems are examined. The tests indicate that the dual-purpose algorithm behaves similarly for solving both flow cases. As a conclusion, it can be claimed that the type of boundary condition definition as well as the proper choice of on/off switches govern the type of compressible or incompressible flow solutions. At the end the authors would like to reemphasize that the results of both compressible and incompressible procedures are obtained within a pure SIMPLE-based incompressible algorithm. In other words, the present algorithm provides a simple strategy that enables the elliptic fluid flow solvers to solve hyperbolic flows.

Acknowledgment

The present work was supported partly by the research center of Sharif University of Technology under Grant SUT-RC-80-4104. It is gratefully acknowledged.

References

[1] Soh, W., and Goodrich, J., "Unsteady Solution of Incompressible Navier–Stokes Equations," *Journal of Computational Physics*, Vol. 79, No. 1, 1988, pp. 113–134.

[2] Mary, I., Sagaut, P., and Deville, M., "Algorithm for Low Mach Number Unsteady Flows," *Computers and Fluids*, Vol. 29, No. 2, 2000, pp. 119–147.

[3] Patankar, S. V., *Numerical Heat Transfer and Fluid Flow*, 2nd ed., Hemisphere, New York, 1996, Chaps. 5, 6.

[4] Van Doormaal, J. P., Raithby, G. D., and McDonald, B. H., "The Segregated Approach to Predicting Viscous Compressible Fluid Flows," *Journal of Turbomachinery*, Vol. 109, No. 2, 1987, pp. 268–277.

[5] Karki, K. C., and Patankar, S. V., "Pressure Based Calculation Procedure for Viscous Flows at All Speeds in Arbitrary Configurations," *AIAA Journal*, Vol. 27, No. 9, 1989, pp. 1167–1173.

[6] Shyy, W., Chen, M. H., and Sun, C. S., "Pressure-Based Multigrid Algorithm for Flow at All Speeds," *AIAA Journal*, Vol. 30, No. 11, 1992, pp. 2660–2669.

[7] Marchi, C. H., and Maliska, C. R., "A Non-Orthogonal Finite-Volume Method for the Solution of All Speed Flows Using Co-located Variables," *Numerical Heat Transfer B*, Vol. 26, No. 3, 1994, pp. 293–311.

[8] Demirdzic, I., Lilek, Z., and Peric, M., "A Collocated Finite Volume Method for Predicting Flows at All Speeds," *International Journal for Numerical Methods in Fluids*, Vol. 16, No. 12, 1993, pp. 1029–1050.

[9] Greyvenstein, G. P., and Meyer, J. P., "Differencing of Density in Compressible Flow for a Pressure-Based Approach," *AIAA Journal*, Vol. 32, No. 3, 1993, pp. 659–661.

[10] Lien, F. S., and Leschziner, M. A., "A General Non-orthogonal Collocated Finite Volume Algorithm for Turbulent Flow at All Speeds Incorporating Second-Momentum Turbulence-Transport Closure, Part 1: Computational Implementation," *Computer Methods in Applied Mechanics and Engineering*, Vol. 114, 1994, pp. 123–148.

[11] Kobayashi, M. H., and Pereira, J. C. F., "Characteristic-Based Pressure Correction at All Speeds," *AIAA Journal*, Vol. 34, No. 2, 1996, pp. 272–280.

[12] Harten, A., Engquist, B., Osher, S., and Chakravarthy, S. R., "Uniformly High Order Accurate Essentially Non-Oscillatory Schemes, III," *Journal of Computational Physics*, Vol. 71, No. 2, 1987, pp. 231–303.

[13] Issa, R. I., and Javareshkian, M. H., "Pressure-Based Compressible Calculation Method Utilizing Total Variation Diminishing Schemes," *AIAA Journal*, Vol. 36, No. 9, 1998, pp. 1652–1657.

[14] Date, A. W., "Solution of Navier–Stokes Equations on Nonstaggered Grid at All Speeds," *Numerical Heat Transfer, Part B*, Vol. 33, 1998, pp. 451–467.

[15] Moukalled, F., and Darwish, M., "A High-Resolution Pressure-Based Algorithm for Fluid Flow at All Speeds," *Journal of Computational Physics*, Vol. 168, No. 1, 2001, pp. 101–133.

[16] Darbandi, M., and Schneider, G. E., "Analogy-Based Method for Solving Compressible and Incompressible Flows," *Journal of Thermophysics and Heat Transfer*, Vol. 12, No. 2, 1998, pp. 239–247; also AIAA Paper 97-0706, Jan. 1997.

[17] Darbandi, M., Schneider, G. E., and Hosseinizadeh, S. F., "Solving Compressible Flow Using SIMPLE Incompressible Procedure," AIAA Paper 2001-2967, June 2001.

[18] Versteeg, H. K., and Malalasekera, W., *An Introduction to Computational Fluid Dynamics; The Finite Volume Method*, Addison Wesley Longman, Reading, MA, 1995, Chap. 6.

[19] Ghia, U., Ghia, K. N., and Shin, C. T., "High-Re Solutions for Incompressible Flow Using the Navier–Stokes Equations and a Multigrid Method," *Journal of Computational Physics*, Vol. 48, No. 3, 1982, pp. 387–411.

[20] Pletcher, R. H., and Chen, K. H., "On Solving the Compressible Navier–Stokes Equations for Unsteady Flows at Very Low Mach Numbers," *Proceedings of the 11th Computational Fluid Dynamics Conference*, AIAA, Washington, DC, 1993, pp. 765–775.

[21] Volpe, G., "Performance of Compressible Flow Codes at Low Mach Numbers," *AIAA Journal*, Vol. 31, No. 1, 1993, pp. 49–56.

[22] Ajmani, K., Ng, W. F., and Liou, M. S., "Preconditioned Conjugate-Gradient Methods for Low-Speed Flow Calculations," AIAA Paper 93-0881, Jan. 1993.

[23] Gartling, D. K., "A Test Problem for Outflow Boundary Conditions-Flow over a Backward-Facing Step, *International Journal for Numerical Methods in Fluids*, Vol. 11, No. 7, 1990, pp. 953–967.

[24] Pepper, D. W., Burton, K. L., Brueckner, F. P., and Blackwell, B. F., "Numerical Simulation of Laminar Flow with Heat Transfer over a Backward Facing Step," *Benchmark Problems for Heat Transfer Codes*, edited by B. Blackwell and D. W. Pepper, HTD-Vol. 222, American Society of Mechanical Engineers, New York, 1992, pp. 21–26.

[25] Morihara, H., and Cheng, R. T., "Numerical Solution of Viscous Flow in the Entrance Region of Parallel Plates," *Journal of Computational Physics*, Vol. 11, No. 4, 1973, pp. 550–572.

[26] Darbandi, M., and Schneider, G. E., "A Benchmark Study for Developing Channel Inlet Flow," AIAA Paper 98-0874, Jan. 1998.

[27] Carvalho, T. M. B., Cotta, R. M., and Mikhailov, M. D., "Flow Development in Entrance Region of Ducts," *Communications in Numerical Methods in Engineering*, Vol. 9, No. 6, 1993, pp. 503–509.

[28] Chen, K. H., and Pletcher, R. H., "Primitive Variable, Strongly Implicit Calculation Procedure for Viscous Flows at All Speeds," *AIAA Journal*, Vol. 29, No. 8, 1991, pp. 1241–1249.

[29] Schwartz, L. W., "A Perturbation Solution for Compressible Viscous Channel Flows," *Journal of Engineering Mathematics*, Vol. 21, 1987, pp. 69–86.